Diamond & Related Materials xxx (xxxx) 114030

Contents lists available at ScienceDirect

Diamond & Related Materials

journal homepage: www.elsevier.com/locate/diamond

Multifunctional CNT-decorated cobalt Iron nanocomposite for efficient photocatalytic dye degradation coupled with potent antibacterial and anticancer activity

Keerthi Ankathi [a], Chouhan Yamuna [a], Anubha Gupta [b], Borlakunta Vanaja [a], Pranay Bhasker Kalakonda [c], Sreenivas Banne [d], Vijay Morampudi [b], Parvathalu Kalakonda [a, e, *]

[a] Department of Physics, Smart Nanomaterial Research Laboratory, Government City College (A), Osmania University, Hyderabad, TG, 500002, India
[b] Department of Biochemistry, University of Hyderabad, Hyderabad, TG, 500046, India
[c] Department of Materials Science and Engineering, North Carolina State University, Raleigh, NC, 27695, USA
[d] Department of Pathology & Immunology, Baylor College of Medicine, Houston, TX, 77030, USA
[e] Saveetha School of Engineering, Saveetha Institute of Medical and Technical Sciences (SIMATS), Chennai, 602105, Tamil Nadu, India

ARTICLE INFO

Keywords:
Green synthesis
CNT-Co-Fe nanocomposite
Multifunctional nanocomposite
Photocatalysis
Antibacterial activity
MTT assay

ABSTRACT

Organic dye pollution, rapidly spreading drug-resistant bacteria, and rising colon cancer incidence are major global health threats. Materials capable of addressing all three challenges simultaneously remain rare. We synthesized a multiwalled carbon nanotube-cobalt-iron (CNT–Co-Fe) nanocomposite using *Murraya koenigii* (MK-curry leaf) extract. Two CNT loadings (2.5 wt% and 5 wt%) were prepared, along with pristine Co—Fe nanoparticles. Under visible light, the 5 wt% CNT-Co-Fe degraded methylene blue (MB) achieving 99% degradation in 60 min, with a rate constant of 0.052 min^{-1} which is 2.6 times faster than that of pristine Co—Fe. The same composite (5 wt% CNT–Co-Fe) fully inhibited enteropathogenic *E. coli* (EPEC) growth (no colonies recovered; > 99.99%, kill at 100 μg/mL) and decreased HCT 116 colon cancer cell viability dose-dependently. The superior performance of the 5 wt% composite is attributed to CNT-mediated electron extraction from Co—Fe, which suppresses charge recombination and enhances radical generation. This trifunctional, green-synthesized CNT–Co-Fe nanocomposite offers a promising single-material platform for water treatment, antibacterial therapy, and anticancer applications.

1. Introduction

Water reused in farming, industry, or daily life demands low cost and effective pollutants or toxic molecules. Green technology has stepped in as a practical solution, especially as many countries now place water reuse high on their policy agenda. Unpredictable rainfall, shortage of freshwater reserves, population growth, and increasing global temperatures have all put a lot of pressure on natural water supplies [1,2]. At the same time, the synthetic dye industry has grown enormously since Perkin's accidental mauveine discovery in 1856 [3,4]. These complex dye molecules not only spoil groundwater but also damage soil [3]. Nanocomposites can fully fragment dye complex molecules, unlike traditional adsorbents [5].

Traditional waste-water treatments such as adsorption, coagulation, and membrane filtration often fail to break down synthetic complex dyes. Advanced oxidation processes system, particularly photocatalysis, offer a more complete removal of complex dye molecules [6–9]. Among all nanotechnology-based solutions, photocatalysis stands out as the most promising method because it completely degrades complex dye molecules rather than just transferring them from one place to another [10–12].

The photocatalysis process works because the catalyst material, when hit by visible light, creates electron-hole pairs (plasmons) [13,14]. These plasmons then react with H_2O and O_2 molecules to produce highly reactive species (ROS) like hydroxyl and superoxide radicals. These radicals attack complex organic dye molecules and break them down into harmless materials (carbon dioxide and water) [2,15].

Despite significant advances in photocatalysis through dye degradation, the development of a single smart nanomaterial capable of simultaneously addressing dye pollutant material, bacterial contamination,

* Corresponding author at: Department of Physics, Smart Nanomaterial Research Laboratory, Government City College (A), Osmania University, Hyderabad, TG, 500002, India.
E-mail address: parvathalu@wpi.edu (P. Kalakonda).

https://doi.org/10.1016/j.diamond.2026.114030
Received 20 June 2026; Received in revised form 20 July 2026; Accepted 29 July 2026
0925-9635/

and cancer cell proliferation remains a formidable challenge [16,17]. While cobalt-iron (Co—Fe) bimetallic nanocomposite have shown promise results due to their narrow bandgap and magnetic properties, their industrial and practical applications are severely hindered by two critical limitations [18,19]: (i) rapid electron-hole recombination within nanoseconds, which wastes most of the light energy before dye molecule breakdown can occur [20], and (ii) severe aggregation tendency due to their magnetic nature, which drastically reduces the available surface area for catalytic reaction [21].

Carbon nanotubes (CNTs) [22] offer a compelling solution to these challenges. Recent studies have demonstrated that CNTs can serve dual roles in nanocomposite systems: as electron superhighways that extract photogenerated electrons and suppress charge recombination, and as physical spacers that prevent nanoparticle agglomeration [18,22,23]. However, most reported CNT-metal oxide composites rely on harsh chemical reducing agents and toxic solvents, limiting their environmental compatibility. Furthermore, studies on multifunctional CNT-based nanocomposites addressing photocatalysis, antibacterial, and anticancer activities simultaneously are extremely rare [24].

To the best of our knowledge as per the literature, no prior study has reported on a green-synthesized CNT-decorated Co—Fe nanocomposite as a three-in-one platform for photocatalytic dye degradation, antibacterial therapy, and anticancer treatment. This research gap is what motivated us to begin our research work [4]. We aimed to develop a single, eco-friendly smart nanocomposite material that could address three major global health threats [25] dye pollution, drug-resistant bacterial infections, and colon cancer with one composite nanomaterial [17,19,26].

In this study, we synthesized CNT-Co-Fe nanocomposites at two different CNT loadings (2.5 wt% and 5 wt%) alongside pristine Co—Fe using a one-pot green synthesis approach with *Murraya koenigii* (curry leaf) extract, which serves as a natural reducing and stabilizing agent [27].We confirmed the structure using UV–vis, FTIR, XRD, and FESEM [26], and tested it for visible-light-driven dye degradation, antibacterial activity against enteropathogenic *E. coli* (EPEC), and anticancer effects on HCT 116 colon cancer cells using the MTT assay [27]. The results, presented below, show that the 5 wt% CNT-Co-Fe nanocomposite achieves 99% complex dye breakdown in 60 min under visible light while also demonstrating potent antibacterial activity and significant anticancer effects a three-in-one performance that makes it a promising candidate for real-world industrial applications.

2. Methods and characterizations

2.1. Materials

$Co(NO_3)_2.6H_2O$, $Fe(NO_3)_3.9H_2O$, MWCNT, Isopropanol (IPA), Methylene blue (MB dye), and acetone solvents were purchased as analytical grade from SRL, India. Fresh Curry leaves (*Murraya koenigii* (MK)) were collected from our institute bio-diversity garden [28,29].

2.2. Synthesis of nanocomposites

Cobalt-iron bimetallic nanoparticles (Co—Fe) were synthesized using our previously reported method with modifications [14]. First, a green extract solution was synthesized by dissolving 1 g of MK extract powder in 100 mL of DI water. In separate vials, $Co(NO_3)_2.6H_2O$, $Fe(NO_3)_3.9H_2O$ salts were each dissolved in 50 mL DI water with equal weights in a stoichiometric ratio. Each salt solution was placed at 80 °C and stirred with 700 rpm for 10 min, followed by ultrasonication for another 10 min. The two salt solutions were then combined in a single vial and the same conditions were applied to the mixture: 80 °C and 700 rpm for 10 min, then ultrasonication for 10 min. Multi-wall carbon nanotubes (MWCNTs) were added to mixed salt solutions at two different weight percentages (2.5 wt% and 5 wt%). The composite mixture was again stirred and sonicated under the same conditions. Next, 30 mL of the green extract solution was added dropwise with the help of standard burette to the composite final solution. The nanocomposite final solution was then dried and calcined at 300 °C for 4 h to obtain a fine powder. Fig. 1 provides a schematic summary of the one-pot green synthesis procedure.

2.3. Characterization of nanocomposites

FE-SEM and EDS were used to analyze morphological features and the elemental composition of the CNT-based Co—Fe BMNP samples. FTIR spectra (400–4000 cm^{-1}) were recorded using the Thermo-Fisher Bruker NEXUS 470 spectrometer. Crystallinity and phase details of the composite samples were extracted with the help of the Shimadzu XRD-7000 diffractometer with Cu Kα radiation wavelength of λ = 0.15418 nm (scanning from 10° to 80°). The optical absorption of the nanocomposite samples was characterized by the Shimadzu UV-1800 double-beam spectrometer.

2.4. Photocatalytic activity

The photocatalytic activity of the nanocomposites was analyzed by dissolving a 10 ppm methylene blue (MB) dye solution in visible light, adding 10 mg of composite catalyst samples to 50 mL of the dye solution. The samples were first placed in a dark region for 20 min to allow the catalyst samples to adsorb the dye, and then they were placed under visible light. The intensity of the MB dye solution was measured using UV–Vis spectroscopy at 664 nm every 15 min. The MB dye degradation was assessed using Eq. (1).

$$\text{Percentage of MB dye degradation} = \left(1 - \frac{C}{C0}\right) \times 100 \quad (1)$$

C_0 represents the initial absorption and C indicates the absorption of dye at different time during the degradation process [18,28].

2.5. Antibacterial activity and anticancer activity

The nanocomposite samples were tested antimicrobial activity and anticancer activity of the using protocol in our previous research work [24]. To ensure reliability, the antibacterial activity (agar well disc diffusion [30] & minimum inhibition concentration [31]) and anticancer activity assays against EPEC and HCT116 colon cancer cells were performed based on the results from the MTT assay [32]. For all assays, overnight cultures of the composite samples were adjusted to an optical density of 1 at 600 nm. In the disc diffusion test, 30 μg of each composite sample was dried onto sterile discs. 10^8 CFU of EPEC (*E. coli*) from

Fig. 1. Schematic illustration of the biosynthesis process for the MK leaf extract-mediated CNT-Co-Fe (2.5 wt% and 5 wt%) nanocomposites.

overnight bacterial culture (OD600nm = 1) were inoculated with 50 μl of the composite sample and were incubated for 24 h at 37 °C. Sterile LB broth and 30 μg of gentamicin were used as negative and positive control respectively. Following 24 h incubation, the conditions were serially diluted, and the triplicates were plated on LB agar plates. The plates were incubated overnight, and post incubation colonies were counted as CFU/mL.

MTT assay was performed to evaluate the cytotoxic activity of the Co—Fe and CNT-Co-Fe composites on human colon cancer cell line, HCT 116 cells. HCT 116 cells were seeded in a 96 well plate with 100 μl of McCoy's media (supplemented with 10% FBS and 1 × Pen Strep) and grown to full confluency at 37 °C in 5% CO_2. 10 μl of the samples were added to the cells and incubated for 24 h at 37 °C in 5% CO_2. Monolayers of cells in the growth media were used as negative control. Following incubation, cells were incubated with 100 μl of MTT solution (5 mg/mL) for 2 h at 37 °C, 5% CO_2. After incubation, MTT was discarded and 100 μl DMSO was added to each well following which OD was measured at 570 nm. The efficacy and safety profile of these CNT-based Co—Fe composite samples should be further explored through in vivo studies to better understand their anti-pathogenic and cytotoxic activity.

3. Results and discussion

3.1. Structural and phase analysis

The X-Ray diffraction (XRD) patterns of pristine Co—Fe nanoparticles and CNT/Co-Fe nanocomposites are indicated in Fig. 2. The pristine Co—Fe bimetallic nanoparticle sample exhibits a sharp reflection at 15.4^0, 19.4^0, 28.5^0, and 41.4^0 (2θ), indexed to a face-centered cubic (FCC) Co—Fe sample. The peak at 41.4^0 corresponding to (110) plane of face centered cubic (FCC) with Co—Fe composite (JCPDS No. 48–1817, a = 3.58–3.62 A^0). No separate reflections from Co or Fe or metal oxide are observed, confirming complete composite formation. For the CNT based Co—Fe composite, two additional peaks appear due to CNT incorporation. The first peak, at 2θ = 13.9^0 with peak intensity, corresponds to the (100) plane, while the second peak at 29.5^0 (JCPDS No. 41–1487, graphitic) [33]. The CNT-specific peaks appear alongside Co—Fe reflections, indicating intact crystal structure after CNT addition.

The crystal structure of the CNT-Co-Fe composite is a multiphase nanocrystalline system. The dominant phase is a face-centered cubic (FCC) Co—Fe sample (JCPDS No. 48–1817). A $CoFe_2O_4$ spinel oxide phase (JCPDS No. 22–1086) forms a partial passivation shell on the composite due to air-exposure during grinding process. Using the Debye Scherrer equation applied to the (110) peak, the average crystallite size decreases from 32.4 nm (pristine Co—Fe) to 18.7 nm (CNT-Co-Fe composite). This decrease suggests that CNTs restrict grain growth. Peak broadening and a 0.15^0 shift towards lower 2θ in the composite sample indicate lattice strain and it might be due to possible electron transfer from Co—Fe to CNTs.

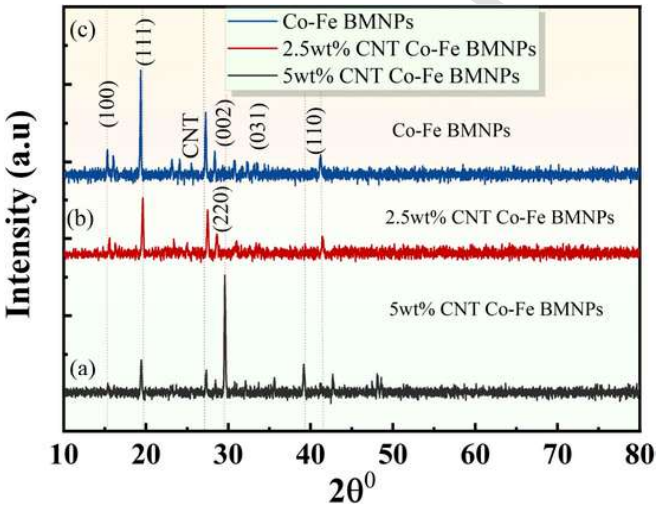

Fig. 2. XRD spectra of pristine Co—Fe and CNT-based Co—Fe nanocomposites.

A slight asymmetry in the FCC (200) peak at 47.5^0 points to minor $(Co, Fe)_3C$ carbide phase (JCPDS No. 26–0450 or 35–0772) at the metal-CNT interface, likely formed via mechano-chemical reaction between the composite sample and carbon support. This unique hierarchical architecture for Co—Fe composite sample & $CoFe_2O_4$ oxide shell anchored on disordered CNTs which is expected to enhance both magnetic anisotropy and catalytic stability, making the composite highly promising for photocatalytic applications. The details of crystallite size equation as per the literature [34] and phase are mentioned in Table.1.

$$D = \frac{0.9\lambda}{\beta cos\theta} \quad (2)$$

3.1.1. Mechanism of CNT-induced grain growth restriction

The reduction in crystallite size from 32.4 nm to 18.7 nm upon CNT addition is attributed to Zener pinning, where CNTs act as physical barriers segregating Co—Fe nanoparticles. The pinning pressure (P_z) exerted by CNTs on grain boundaries is given by:

$P_z = 3\gamma f/2r$.

where γ is the grain boundary energy, f is the volume fraction of CNTs, and r is the CNT radius. As CNT loading increases, the pinning pressure increases, leading to more effective grain size suppression. Additionally, CNTs provide alternative nucleation sites, promoting heterogeneous nucleation and resulting in a higher density of smaller crystallites. The entangled CNT network also constrains atomic diffusion during calcination, effectively "freezing" the smaller crystallite size.

3.2. Surface chemistry and functional groups: FTIR

Fig. 3 presents FTIR spectra obtained from both the MK extract and the composites. A wide broad peak observed close to 3350 cm^{-1}, appeared in the MK extract which is typical for O—H [35] stretching coming from phenolic and hydroxyl groups. Another distinct vibration band peak located at 1630 cm^{-1} was also noted, which represent to the C═O stretching for amides [36]. Among successful synthesis of Co—Fe composite, a new low-frequency bands appeared in the region from 500 and 600 cm^{-1}, which corresponds to Metal-Oxide-Metal stretching vibrations (Co—O and Fe—O) [36], confirming composite formation. In the 2.5 wt% CNT composite sample, the O—H and C═O bands remained visible but with diminished intensity, indicating that phytochemicals still anchored on the surface of nanocomposites [37]. At 5 wt% CNT loading, further suppression of these bands was observed, suggesting stronger CNT-nanoparticle surface interaction (wrapped a layer on the surface of nanocomposite). No new vibration bands were detected in the composites, implying that CNT incorpora-

Table 1
Crystallite size and phase details of CNT based Co—Fe composites.

Phase	Lattice parameters (A^0)	2θ	(hkl)	Crystallite size	JCPDS No.
Co-Fe FCC	a = 3.59 ± 0.02	41.4^0	(110)	20.1 ± 2	48–1817
$CoFe_2O_4$ (spinel)	a = 8.39	30.4^0	(220)	10.2 ± 1.0	22–1086
CNT (graphitic, disordered)	Interlayer = 3.78 ± 0.05	29.5^0	(002)	3–5 (broad)	41–1487
$(Co, Fe)_3C$ Carbide	a = 4.52, b = 5.09,c = 6.74	37.8	(031)	7.0 ± 1.0	35–0772/26–0450

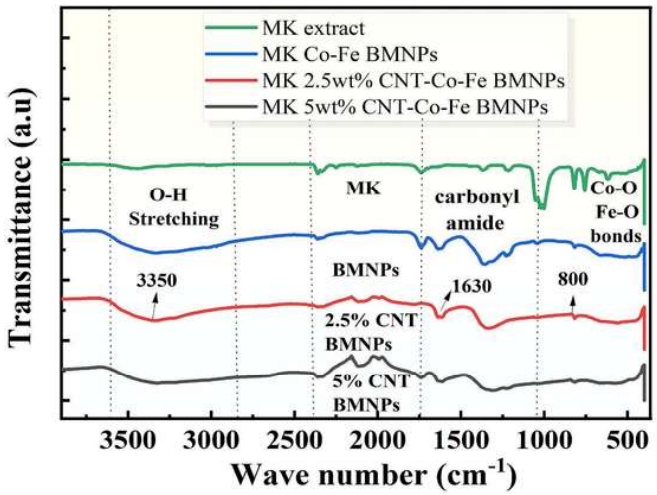

Fig. 3. FTIR spectra of MK leaf extract, Co—Fe, Co—Fe composites with 2.5 wt% and 5 wt% carbon nanotubes (CNTs).

tion did not chemically change the Co—Fe composite core. Since both O—H and C=O bands remained after CNT addition, it implied that MK's phytochemicals were surface-bound. The gradual decreasing of these band intensities as the CNT fraction rose from 2.5 to 5 wt% was most likely due to a physical anchoring effect, rather than actual removal or displacement of the surface functional groups. This mechanism is supported by the absence of new vibrational modes in the composites. The retention of metal oxide bands in all samples confirms that the Co—Fe composite structure remains intact. Collectively, the FTIR analysis indicate that CNT acts as an electronically conductive filler without sacrificing the bio-derived surface chemistry essential for dispersion [38] and stability [38].

3.3. Morphology, microstructure, and elemental distribution: FESEM

FE-SEM was used to know the surface morphology and microstructure of pristine Co—Fe and CNT Co—Fe composites (Fig. 4). Pristine Co—Fe (Fig. 4: A-B) formed irregular, aggregated granular particles with uneven distribution. The nanoparticle boundaries were not clearly marked, indicating strong interparticle attraction typical of uncapped or partially MK extract capped Co—Fe systems. EDS confirmed the presence of both Co and Fe in the pristine sample (Fig. 4B). 2.5 wt% CNTs Co—Fe composite (Fig. 4: C—D) sample observed noticeable micro-structure. CNTs features were visible around the surface of Co—Fe, and nanoparticles clustering decreased moderately after addition of CNTs. At 5 wt% CNTs loading (Fig. 4: *E*-F), the Co—Fe composites dispersed more uniformly throughout the CNT network, with clustering suppressed further than in the pristine Co—Fe sample. Nonetheless, small local clusters persisted, indicating that 5 wt% CNTs improves degree of dispersion but does not entirely prevent agglomeration. Image analysis of FE-SEM micrographs (n = 50 particles per sample) revealed a mean particle diameter of 120 ± 40 nm for pristine Co—Fe, compared to 80 ± 25 nm for the 5 wt% CNT composites. The reduction in particle size indicates that CNTs effectively suppress nanoparticle aggregation and coalescence during green synthesis process.

XRD analysis of pristine Co—Fe composite revealed low-intensity peaks, suggesting poor crystallinity or small particle size - consistent with the aggregated morphology seen in FE-SEM. The reduced aggregation observed at 5 wt% CNTs loading supports that CNTs act as physical barriers against nanoparticle coalescence [39]. The improved dispersion at 5 wt% CNTs correlates with enhanced photocatalytic, antibacterial, and anticancer activity, likely through increased generation of reactive oxygen species (ROS).

3.4. Optical properties (UV–Vis Spectroscopy)

The optical absorption measurements for both the pristine Co—Fe and 5 wt% CNT Co—Fe composite samples were carried out over a region from 200 to 800 nm (Fig. 5). A wide absorption feature appeared in the 270 and 420 nm for both the composites. This band arises from surface plasmon resonance of Co—Fe composite combined with electronic transitions [40]. Lower absorption values were recorded the 5 wt% CNT Co—Fe composite relative to the pristine Co—Fe sample. This decline is attributed to an optical quenching effect by the CNTs network [41]. Tauc plots obtained from the absorption spectra (Fig. 6) were used to measure the direct and indirect optical bandgap. The direct bandgap of the pristine Co—Fe sample was approximately 3.0 eV, whereas the 5 wt% CNT composites yielded a higher direct bandgap of roughly 3.2 eV (Fig. 6A). For the indirect bandgap, the pristine sample gave 2.9 eV compared to 3.0 eV for the CNT-containing sample (Fig. 6B). Both bandgaps moved to higher energies upon CNT addition, a shift that may result from quantum confinement effects [42].

The addition of CNTs into Co—Fe system did not merely preserve the optical activity but systematically altered both the absorption intensity and the fundamental optical bandgaps [42]. The reduced absorbance combined with a larger optical bandgap in the 5 wt% CNT Co—Fe composite sample pointed to a non-trivial electronic interac-

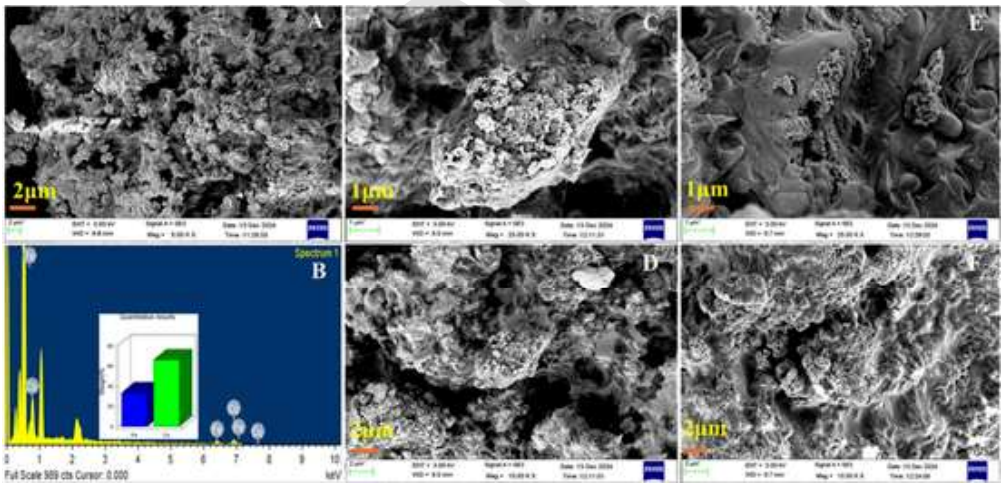

Fig. 4. FE-SEM images of (A-B) pristine Co—Fe composite showing aggregation and elemental analysis (EDS); (C—D) 2.5 wt% CNTs composite with partial CNTs decoration and reduced clustering; (E-F) 5 wt% CNTs composite exhibiting improved dispersion.

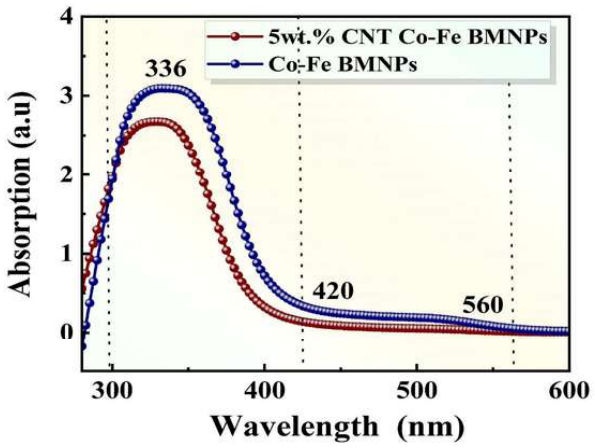

Fig. 5. UV–Vis absorption spectra of pristine Co—Fe and 5 wt% CNT-based Co—Fe nanocomposites.

tion between the CNTs and the system. When CNTs wrap around nanoparticles, they restrict the motion of electrons in the composite system. These findings provided a clear rationale for tailoring the optical properties of hybrid nanostructures through controlled CNTs loading, making the 5 wt% CNT Co—Fe composite a promising candidate for optoelectronic devices requiring tunable bandgaps and controlled light absorption [43].

Using Tauc plot analysis with $(\alpha h\nu)$ [2] for direct and $(\alpha h\nu)^{1/2}$ for indirect bandgaps, with proper baseline correction and zeroing of the y-axis. The observed increase in the optical direct bandgap from ~3.0 ± 0.04 eV for pristine Co—Fe to ~3.2 ± 0.05 eV for the 5 wt% CNT-Co-Fe composite and indirect bandgap 2.9 ± 0.05 eV for pristine Co—Fe to 3 ± 0.03 eV for the 5 wt% CNT-Co-Fe composite, appearing enhanced photocatalytic activity, is a known phenomenon for CNT-metal oxide nanocomposites. The bandgap values in the visible range are consistent with the observed visible-light photocatalytic activity. This increase can be attributed to quantum confinement effects and the formation of a Schottky barrier at the Co-Fe/CNT interface. The enhanced photocatalytic performance arises not from a narrower bandgap, but from the superior charge separation and transfer capabilities offered by the CNTs. The metallic CNTs act as an efficient electron sink, rapidly extracting photogenerated electrons from the Co—Fe and dramatically suppressing electron-hole recombination. This is further supported by the enhanced degradation rates observed by increasing CNT loading. Thus, the composite material benefits from a larger driving force for the generation of reactive radicals due to the longer lifetime of the charge carriers, a key factor that outweighs the effect of a slight bandgap increase. The average direct bandgap of 3.1 ± 0.05 eV suggests primarily UV absorption, the presence of an indirect bandgap (2.95 ± 0.05 eV), broad visible absorption tail, and SPR effects collectively enable visible-light photocatalytic activity. The photogenerated charge carriers utilize sub-bandgap excitation pathways facilitated by the multi-metal synergy.

3.5. Photocatalytic activity

The catalytic performance of the green-synthesized Co—Fe and CNT-Co-Fe composite catalyst to break down MB dye was investigated under visible light exposure. The pristine Co—Fe, CNT (2.5 wt%, 5 wt%) based Co—Fe composite samples were evaluated and analyzed (Fig. 7). The degradation time was monitored for 75 min with measurements taken at 15 min intervals for pristine Co—Fe sample, 2.5 wt% CNT, and every 10 min interval for 5 wt% CNT Co—Fe composite sample. Table 2 presents the degradation percentage for all catalyst samples as the function time.

Among three Co—Fe & CNT-Co-Fe catalyst samples, the pristine Co—Fe catalyst sample achieved 78% degradation against the MB dye within 60 min. Introducing CNTs increased the degradation efficiency: the 2.5 wt% CNT composite reached 85%, and the 5 wt% CNT composites reached 99% over the same period. Among the three composite samples, 5 wt% CNT-Co-Fe composite degraded MB fastest and effectively. Calculated rate constant (0.052 min^{-1}) was 2.6 that of pristine Co—Fe sample. This enhanced performance can be traced to three factors [3]: a broader bandgap, suppressed charge recombination, and reduced Co—Fe nanoparticle aggregation The order of catalytic performance remained consistent throughout the experiment (5 wt% CNT > 2.5 wt% CNT > pristine Co—Fe sample) at every measured time. Recent research work reported that their $CoFe_2O_4$/g-C_3N_4 nanocomposite containing 25 wt% g-C_3N_4 achieved complete MB degradation (100%) after 180 min using a catalyst dosage of 400 mg/L. In contrast, the 5 wt% CNT-Co-Fe nanocomposite system in the present study reached 99% (approximately 100%) degradation in only 60 min with a substantially lower catalyst quantity of 30 mg. The potential performance of the 5 wt% CNT-Co-Fe composite system is attributed to the metallic nature of the Co—Fe composite, which provides higher electrical conductivity than the Co—Fe pristine sample, thereby facilitating more efficient charge carrier separation.

The dye breakdown data were fitted to a pseudo-first-order kinetic model using the Langmuir–Hinshelwood approach. For pristine Co—Fe sample, the calculated rate constant was k = 0.02 min^{-1} and 2.5 wt% CNT-Co-Fe composite raised that to 0.043 min^{-1}. The 5 wt% CNT composites provided 0.052 min^{-1} which was 2.6 times faster than that of pristine Co—Fe sample. All three R^2 values stayed above 0.97, confirming the model fits well, indicating the model provided good de-

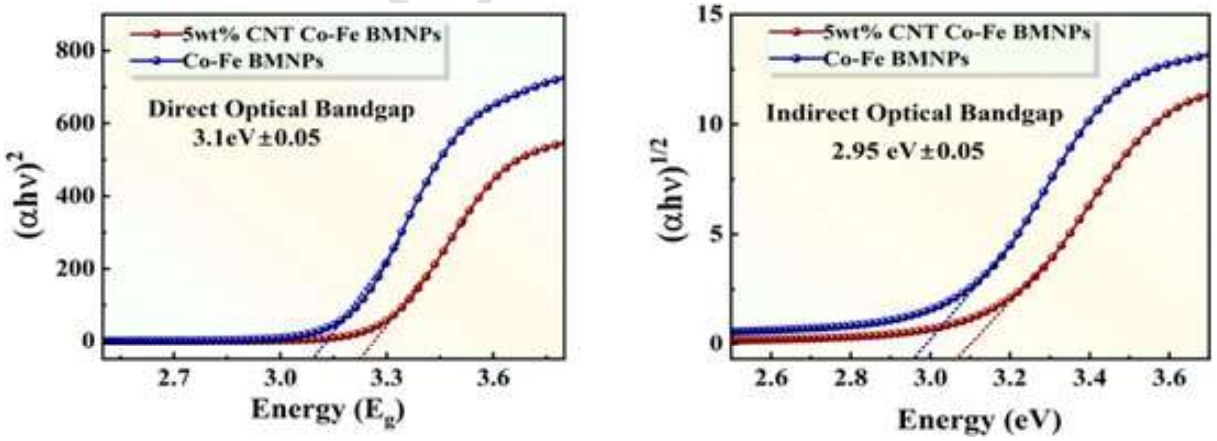

Fig. 6. Tauc plots analysis of pristine Co—Fe, and 5 wt% CNT-based Co—Fe nanocomposites.

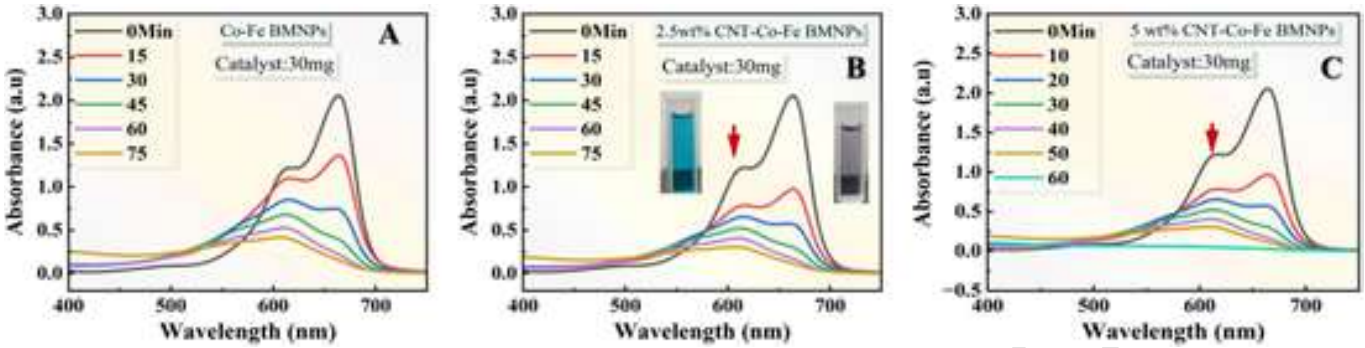

Fig. 7. UV–Vis spectral changes of MB dye (10 ppm) recorded 15 min (10 min for 5 wt% CNT Co—Fe composite) time interval during visible light photocatalysis with 30 mg catalyst. (A) Pristine Co—Fe. (B) 2.5 wt% CNT-Co-Fe composite. (C) 5 wt% CNT-Co-Fe composites. The progressive decline of the 664 nm absorption band confirms dye mineralization without new intermediate peaks.

Table 2
MB dye degradation (%) over time for pristine Co—Fe, 2.5 wt% CNT-Co-Fe, and 5 wt% CNT-Co-Fe.

S. No	Time interval	Co-Fe	2.5wt%CNT Co-Fe	5 wt% CNT Co-Fe
1	10	19 ± 0.8	33 ± 0.3	44 ± 0.8
2	30	57 ± 0.7	70 ± 0.6	75 ± 0.5
3	50	67 ± 0.5	77 ± 0.9	86 ± 0.5
4	60	78 ± 0.9	85 ± 0.7	99 ± 0.8

scription of the experimental data based on the Langmuir-Hinshelwood [44] mechanism (Fig. 8) [44].

$$\ln\left(\frac{C}{C0}\right) = -kt \tag{3}$$

where C represents the dye concentration at time t, C_0 is the initial concentration, k is the rate constant (min^{-1}), and 't' is the irradiation time. Plots of $\ln(C/C_0)$ versus time yielded linear fits with R^2 values exceeding 0.97 for all three composite samples, confirming pseudo-first-order kinetics.

The systematic increase in rate constants with CNT loading indicates that carbon nanotubes actively involve in the photocatalytic process rather than serving as passive CNTs fillers. This effective enhancement was interpreted to high electrical conductivity (CNTs) and the direct addition of CNTs into the Co—Fe system creates efficient electron transport pathways that are absent in the physically mixed system. While recycling and stability experiments were not performed in this study due to equipment limitations, all experiments were repeated independently at least three times to confirm reproducibility. Future work will include 5-cycle photocatalytic recycling tests and 6-month stability monitoring to evaluate the practical applicability of the CNT-Co-Fe nanocomposite for real-world wastewater treatment.

Fig. 9A and B illustrate the basic mechanism involved during photocatalytic process under visible and when visible light reaches the catalyst surface, the absorbed energy promotes an electron from the low energy band to the high energy (conduction) band, leaving a hole in the valence band [45].

3.5.1. *Theoretical basis for the proposed mechanism*

The proposed mechanism is grounded in established semiconductor photocatalysis principles. The Co—Fe composite possesses a direct bandgap of ~2.95 eV, enabling visible light absorption (λ > 420 nm). When CNTs are introduced, a Schottky barrier forms at the Co-Fe/CNT interface due to the work function difference between metallic Co—Fe (~4.8 eV) and semimetallic CNTs (~4.5 eV). This barrier facilitates electron transfer from the Co—Fe conduction band to the CNT network, as described by the following sequence:

$$Co - Fe + h\nu \rightarrow Co - Fe\ \left(e^- + h^+\right)$$
$$e^-\ (Co\text{▬}Fe) \rightarrow e^-\ (CNT)$$
$$e^-\ (CNT) + O_2 \rightarrow \bullet O_2^-$$

$$h^+\ (Co\text{▬}Fe) + H_2O \rightarrow \bullet OH + H^+$$

The high electrical conductivity of CNTs enables rapid electron transport, extending charge carrier lifetime from nanoseconds (in pris-

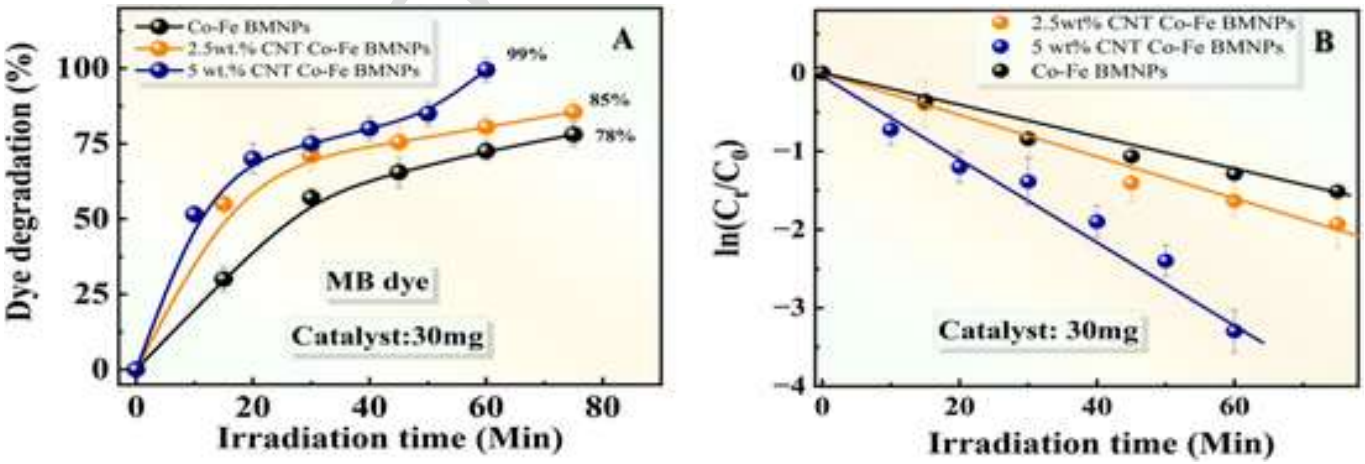

Fig. 8. (A) Time-dependent degradation of MB dye (10 ppm, 30 mg catalyst) under visible light. (B) Pseudo-first-order kinetic plots for pristine Co—Fe, 2.5 wt% CNT Co—Fe composite, and 5 wt% CNT Co—Fe composites.

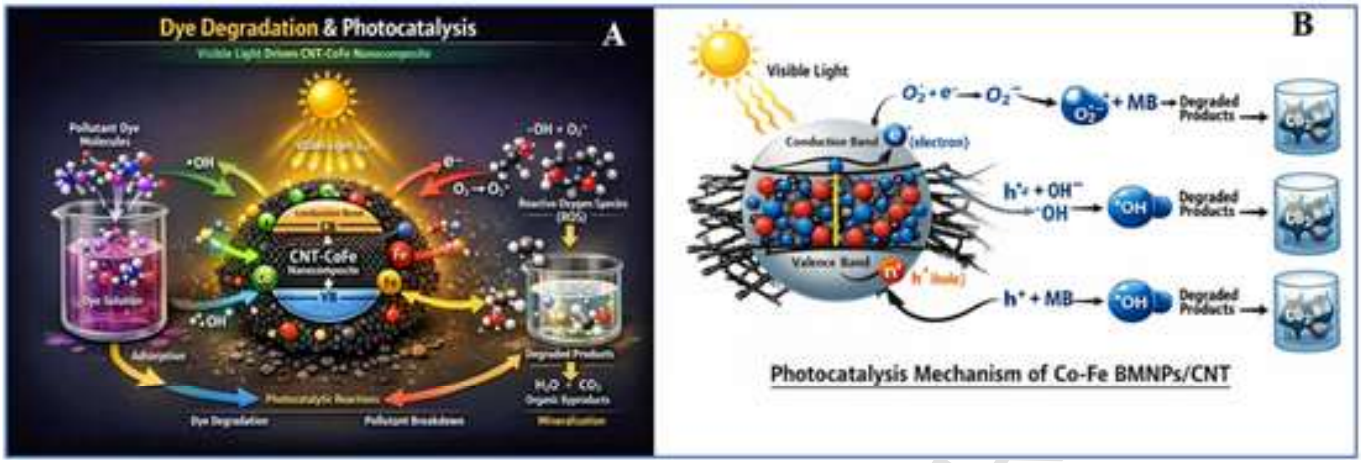

Fig. 9. A &B. Proposed photocatalytic mechanism of CNT-Co-Fe nanocomposite under visible light irradiation.

tine Co—Fe) to microseconds (in CNT-Co-Fe composite), as evidenced by the 2.6-fold increase in degradation rate constant.

In the pristine Co—Fe composite sample, electron-hole pairs recombine quickly within fraction of nanoseconds before they can participate in any chemical reaction [18]. This explains why the pristine Co—Fe sample achieved only 78% degradation against MB dye after 60 min. When CNTs are added at 2.5 wt%, they act as a physical pathway for electrons to escape. An electron generated in the Co—Fe composite transfers into the nearby CNTs network, which conducts it away from the hole. By keeping the two charge carriers apart, this process increases the lifetime of each pair. The electron on the CNTs surface then reacts with dissolved oxygen in water to form superoxide radicals ($O_2\bullet^-$), while the hole remaining on the Co—Fe surface reacts with water or hydroxide ions to produce hydroxyl radicals (•OH) [41]. Both reactive species attack the MB dye and break toxic molecules. The 2.5 wt% CNT Co—Fe sample showed improved performance (85% degradation at 60 min and 99% by 60 min) because more electron-hole pairs survived long enough to generate these reactive species (do not recombine). As shown Table S1 (supplementary) table, the 5 wt% CNT-Co-Fe nanocomposites synthesized in this study demonstrates superior photocatalytic performance compared to recently reported CNT-metal oxide systems. The composite achieves 99% degradation of MB in just 60 min with a rate constant of 0.052 min^{-1}, which is significantly higher than that of other CNT based metal oxide systems [34,46–49] (shown in Table S1). The enhanced performance of our material can be attributed to several factors: (i) the metallic nature of the Co—Fe composite provides higher electrical conductivity than ferrite systems, facilitating efficient charge carrier separation; (ii) the green synthesis approach using *Murraya koenigii* extract yields nanoparticles with unique surface chemistry and defect structures that enhance radical generation; and (iii) the optimized CNT loading (5 wt%) provides an optimal balance of electron extraction and surface accessibility for dye adsorption [20] [21]., This comparison highlights the novelty and practical potential of our green-synthesized CNT-Co-Fe nanocomposite for wastewater treatment applications. The Fig. 9A & B illustrates whole process of mechanism: visible light hits the CNT-Co-Fe nanocomposite, electrons travel through the CNT network, reactive radicals form at the surface, and the dye molecules in solution are broken down into clean water and harmless byproducts as mentioned below. The order of performance (5 wt% CNT > 2.5 wt% CNT > pristine Co—Fe sample) remained unchanged at every measured time point, confirming that higher CNT loading consistently improves charge separation and degradation efficiency.

3.6. Antibacterial activity

The disc diffusion assay revealed a clear distinction in antibacterial behavior among the three samples (pristine Co—Fe, 2.5 wt% & 5 wt% CNT -Co-Fe composite) against *E coli*, as shown in Fig. 10A and B. The MK leaf extract did not show any free zone of inhibition, while the positive control gentamicin showed a cleared zone area of approximately

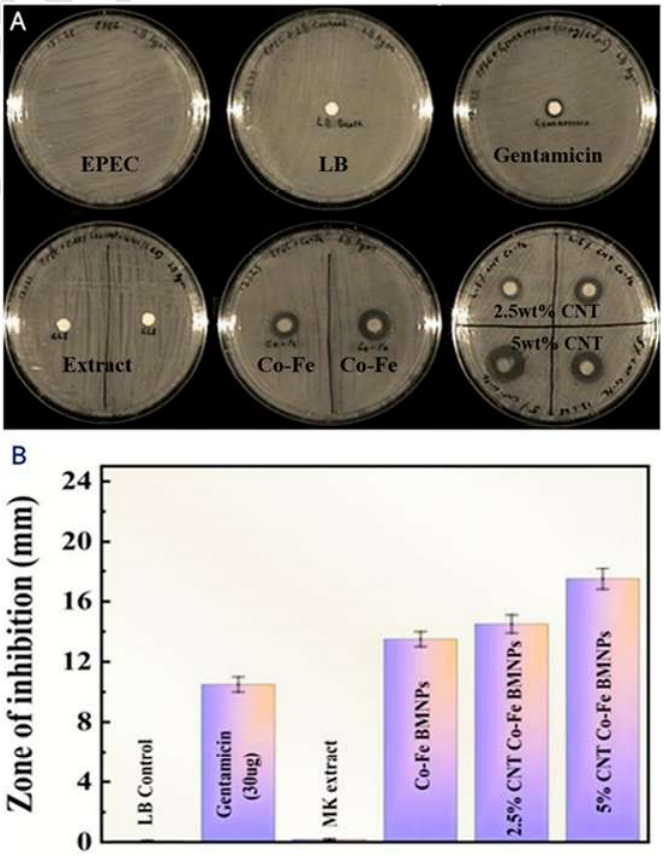

Fig. 10. (A). Representative disc diffusion agar plates showing zones of inhibition against EPEC for LB broth (negative control), gentamicin (positive control), Curry leaf extract, Co—Fe, 2.5 wt% CNT Co—Fe, and 5 wt% CNT Co—Fe composites. (B) Quantitative bar graph of zone diameters (mm) measured after overnight incubation at 37 °C. Error bars represent standard deviation of triplicate measurements. ***$p < 0.001$ versus negative control.

10.5 mm. Pristine Co—Fe, 2.5 wt% CNT Co—Fe and 5 wt% CNT Co—Fe composites samples produced high clear zones of inhibition ranging from 13 to 20 mm (larger than the standard gentamicin), with the CNT-incorporated samples showing marginally larger diameters than the standard gentamicin sample. These results were confirmed by quantitative measurements with help of the direct inhibition assay presented in Fig. 11A and B, where the MK leaf extract again did not show any reduction in bacterial counts remaining at the initial inoculum of approximately 10^6 to 10^8 CFU/mL, whereas pristine Co—Fe, 2.5 wt% CNT Co—Fe, and 5 wt% CNT Co—Fe composites each reduced significantly viable colonies to below the detection limit of 10^2 CFU/mL, corresponding to killing efficiency about 99.9% (bactericidal efficacy). Pure CNT control experiments were not included in this study, as the primary objective was to demonstrate the synergistic performance of the CNT-Co-Fe composite system. However, the significantly higher antibacterial activity of the CNT-Co-Fe composites (inhibition zones of 13–20 mm, >99.99% kill) compared to literature-reported values for pure CNTs (typically 5–10 mm zones, ~90–95% kill at similar concentrations) provides strong indirect evidence for synergy. Pure CNTs are known to exhibit antibacterial activity through physical membrane disruption and low-level ROS generation, but their efficacy is considerably lower than that of metal oxide-CNT composites. Future work will include systematic pure CNT control experiments to quantitatively establish the individual contributions of CNTs and Co—Fe nanoparticles to the overall antibacterial activity [50].

The basic mechanism of this potent activity lies in the surface chemistry and interfacial interactions of the Co—Fe and CNT-Co-Fe composites with the Gram-negative bacterial cell [51]. This genotoxic insult activates the ATM kinase pathway with DNA damage triggers cell cycle arrest. Simultaneously, the nanoscale dimensions and high aspect ratio of the CNT-Co-Fe nanocomposites enable direct physical disruption of the EPEC bacteria strain [17], outer membrane through adhesion, local deformation, and pore formation, leading to loss of selective permeability and leakage of intracellular contents [51]. Once internalized, the reactive oxygen species (ROS) and released Co^{2+} and Fe^{3+} ions attack multiple intracellular targets including DNA through strand breaks and base modifications [24], proteins through carbonylation and crosslinking, and metabolic enzymes through inactivation of iron-sulphur clusters, collectively overwhelming the bacterial antioxidant defences and causing irreversible cell death as evidenced by the complete absence of colony formation [14]. The significantly higher activity of CNT-Co-Fe composites confirms synergy, where CNTs enhance Co—Fe ROS generation while Co—Fe provides additional mechanisms (metal ion release, Fenton chemistry) for potent bactericidal efficacy (no colonies recovered). The antibacterial efficacy of all composites is summarized in Table.3.

3.7. Cytotoxicity of nanoparticles on cancer cell

The anticancer activity of pristine Co—Fe, 2.5 wt% CNT Co—Fe, and 5 wt% CNT Co—Fe composites against HCT 116 human colon carcinoma cells, assessed by MTT assay across a concentration gradient of 0.625–100 μg/mL (Fig. 12), followed a distinctly concentration-dependent pattern [52]. All tested samples MK leaf extract, Co—Fe, 2.5 wt% CNT Co—Fe, and 5 wt% CNT Co—Fe composites induced a progressive decline in cell viability with 2.5 wt% CNT Co—Fe composite exhibiting the most potent effect, reducing viability to approxi-

Table 3
Antibacterial activity details of pristine Co—Fe, 2.5 wt% CNT Co—Fe, and 5 wt% CNT Co—Fe composite nanomaterials against EPEC strain.

S. No	Disc diffusion assay (mm)	Direct inhibition assay (CFC/ml)
LB control (DDA)/EPEC (DIA)	0	3.4×10^9
MK leaf extract	0	3.4×10^9
Co-Fe	13 ± 0.8	5000
2.5 wt% CNT Co—Fe composites	16 ± 1.5	0
5 wt% CNT Co—Fe composites	**20 ± 2.5**	**0**
Gentamicin	10.5 ± 0.5	1.6×10^9

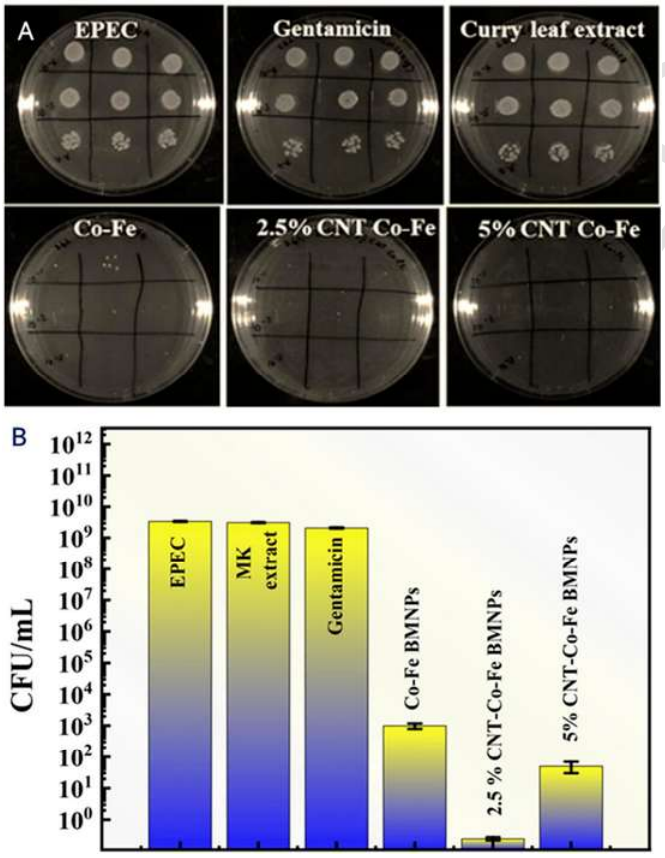

Fig. 11. (A) Representative agar plates showing bacterial colonies after direct inhibition assay of EPEC treated with the indicated formulations for 24 h. (B) Quantitative CFU/mL values plotted on a logarithmic scale. The dashed line indicates the limit of detection (10^2 CFU/mL). ***p < 0.001 versus untreated control.

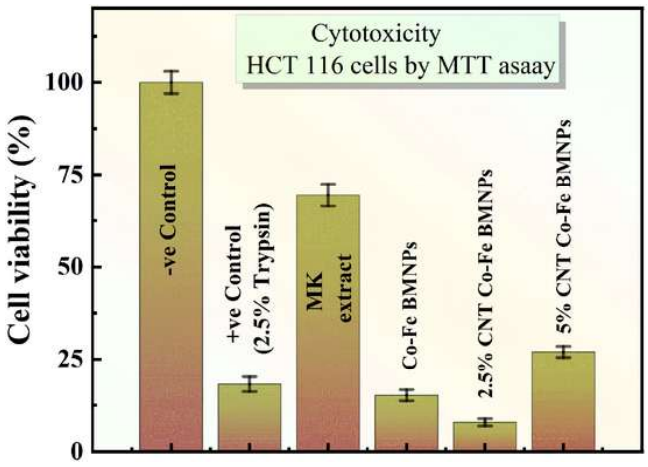

Fig. 12. MTT assay results showing percentage viability of HCT 116 colon cancer cells after 24 h treatment with increasing concentrations (0.625–100 μg/mL) of Curry leaf extract, Co—Fe, 2.5 wt% CNT Co—Fe, and 5 wt% CNT Co—Fe composites. Data are presented as mean ± SD (n = 3). *p < 0.05, **p < 0.01, ***p < 0.001 versus untreated control.

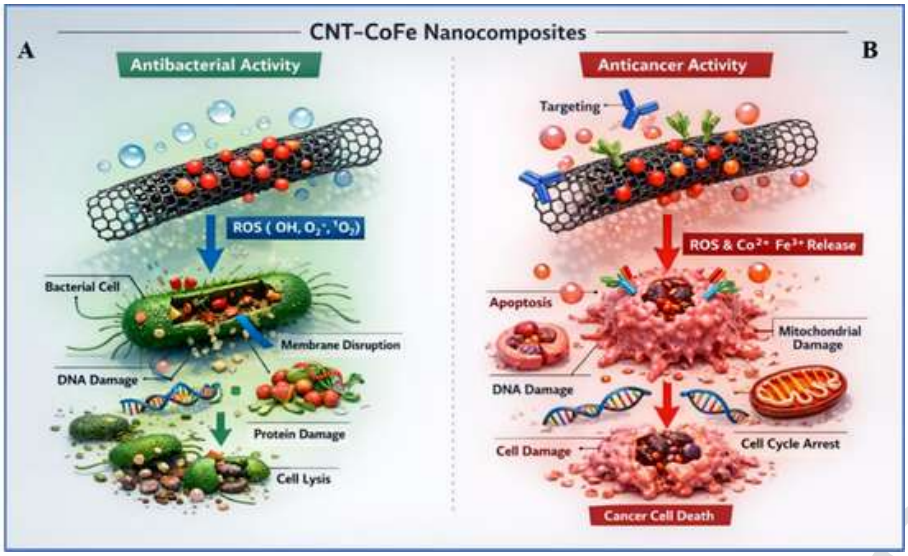

Fig. 13. (A &B). Proposed mechanistic schematic illustrating the dual antibacterial and anticancer pathways.

mately 10–15% of the pristine control at the highest dose. 5 wt% CNT Co—Fe composites showed slightly lower activity than 2.5 wt% CNT Co—Fe composite samples which might be attributed to agglomeration effects and reduced ROS release.

Fig. 13A illustrates how the Co—Fe nanocomposite kills EPEC bacteria using two simultaneous attack routes. This dual strategy allows the material to get around standard resistance mechanisms found in many bacteria. First, the Co—Fe composite surface catalyzes the generation of a burst of ROS, •OH, O_2^-, and singlet oxygen (O_2). These species simultaneously oxidize membrane lipids, denature surface proteins, and penetrate the cell to fragment genomic DNA. Second, the high aspect ratio of the CNTs acts as physical nano-knives: upon contact, they distort and puncture the Gram-negative outer membrane, causing unrepairable leakage of cytoplasmic contents. Critically, the CNT network also shuttles electrons to sustain prolonged ROS production, ensuring that oxidative damage outpaces bacterial repair mechanisms. The 2.5 wt% CNT-Co-Fe composite showed the most potent anticancer effect (10–15% viability at 100 μg/mL), while the 5 wt% composite exhibited slightly lower activity. The result is rapid, multilocus cell lysis not merely growth inhibition making resistance evolution highly unlikely.

In the tumor micro-environment, the CNT-Co-Fe nanocomposite leverages the increased permeability and retention (EPR) effect for passive accumulation (Fig. 13B). Following internalization via CNT-mediated membrane wrapping, the construct releases Co^{2+} and Fe^{3+} ions within endosomal compartments. These ions drive Fenton chemistry, generating a burst of mitochondrial ROS. The ensuing oxidative stress opens the mitochondrial permeability, leading to outer membrane permeabilization and cytosolic release of cytochrome. This triggers the apoptosome cascade and activates executioner caspases, committing the cell to apoptosis. Concurrently, a fraction of Co^{2+} and Fe^{3+} translocate to the nucleus, inducing double-strand breaks and oxidative base lesions. The CNT component enhances each step due to its conductivity sustains the oxidative burst, its high surface area maximizes metal loading, and its elongated shape accelerates uptake transforming a moderate phytochemical-like effect into a potent, dual-compartment cancer cell kill. This is attributed to agglomeration effects and the CNT shielding effect. This limits or regulate intracellular delivery and ROS generation within cancer cells. At higher loading, excess CNTs form a physical barrier around Co—Fe nanoparticles, partially blocking Co^{2+} and Fe^{3+} ion release. These ions are essential for Fenton-chemistry-driven mitochondrial ROS generation and apoptosis induction. The shielding reduces available metal ions for radical generation, diminishing cytotoxicity. This phenomenon, observed in other CNT-metal oxide systems, highlights the need for optimal CNT loading: 5 wt% balances high photocatalytic and antibacterial activity, while 2.5 wt% optimizes anticancer efficacy where metal ion release is critical.

4. Conclusion

We successfully synthesized CNT-Co-Fe composites that serve as a tri-functional platform for dye degradation, bacterial disinfection, and cancer cell cytotoxicity within a single, eco-friendly composite material system. 5 wt% CNT-Co-Fe composite delivered superior performance across all tested applications. Photo-catalytically, the 5 wt% CNT Co—Fe composites achieved 99% MB dye degradation within 60 min under visible light, with a pseudo-first-order rate constant of 0.052 min^{-1}, which is 2.6-fold higher than that of pristine Co—Fe (0.02 min^{-1}). The 5 wt% CNT-Co-Fe composite produced inhibition zones of 20 ± 2.5 mm against enteropathogenic *E. coli* strain substantially larger than the standard gentamicin control (10.5 ± 0.5 mm) and reduced viable bacterial counts below the detection limit (10^2 CFU/mL), representing >99.9% bactericidal efficacy. Anticancer evaluation against HCT 116 colon carcinoma cells revealed concentration-dependent cytotoxicity, with the 2.5 wt% CNT Co—Fe composite showing the most pronounced effect (10–15% viability at 100 μg/mL), whereas the 5 wt% CNT-Co-Fe composite exhibited slightly reduced activity. The 5 wt% CNT-Co-Fe composite showed balanced high photocatalytic and antibacterial efficacy with appreciable anticancer activity, making it the optimal candidate for integrated wastewater remediation and biomedical application.

CRediT authorship contribution statement

Keerthi Ankathi: Formal analysis, Data curation. **Chouhan Yamuna:** Formal analysis, Data curation. **Anubha Gupta:** Formal analysis, Data curation. **Borlakunta Vanaja:** Formal analysis, Data curation. **Pranay Bhasker Kalakonda:** Formal analysis, Data curation. **Sreenivas Banne:** Formal analysis, Data curation. **Vijay Morampudi:** Resources, Methodology, Conceptualization. **Parvathalu Kalakonda:** Writing – review & editing, Writing – original draft, Supervision, Project administration, Conceptualization.

Ethical approval

The internal review board committee of our lab stated that no ethical approval was required for this study as it did not involve human or animal subjects.

Funding

No funding was received for this project.

Uncited references

[53,54]

Declaration of competing interest

The authors declare that they have no known competing financial interests or personal relationships that could have appeared to influence the work reported in this paper.

Data availability

Data will be made available on request.

Appendix A. Supplementary data

Supplementary data to this article can be found online at https://doi.org/10.1016/j.diamond.2026.114030.

References

[1] S. Hamed Latef, A. Jwaid, A comprehensive review of environmental and health risks of textile dyes and strategies for eco-safe remediation, IOP Conf. Ser. Earth Environ. Sci. 1545 (1) (2025) 012109, https://doi.org/10.1088/1755-1315/1545/1/012109.

[2] G. Kavitha, M. Govindhan, S. Premkumar, Dye pollution and its implications for human health, aquatic ecosystems, and sustainable wastewater treatment: a comprehensive review, J. Water Process Eng. 80 (2025) 109071, https://doi.org/10.1016/j.jwpe.2025.109071.

[3] D. Patel, A. Singh, S.R. Ambati, R.S. Singh, R.K. Sonwani, An overview of recent advances in treatment of complex dye-containing wastewater and its techno-economic assessment, J. Environ. Manag. 370 (2024) 122804, https://doi.org/10.1016/j.jenvman.2024.122804.

[4] A. Khatua, A. Prasad, E. Priyadarshini, A.K. Patel, A. Naik, M. Saravanan, H. Barabadi, L. Ghosh, B. Paul, R. Paulraj, R. Meena, Emerging antineoplastic plant-based gold nanoparticle synthesis: a mechanistic exploration of their anticancer activity toward cervical cancer cells, J. Clust. Sci. 31 (6) (2020) 1329–1340, https://doi.org/10.1007/s10876-019-01742-1.

[5] P. Andryskova, R. Prucek, Multimetallic nanostructures: innovations and applications in environmental remediation, biosensing, and medical technologies, Nanoscale 18 (6) (2026) 3004–3017, https://doi.org/10.1039/D5NR02086G.

[6] N.M. Hosny, I. Gomaa, M.G. Elmahgary, Adsorption of polluted dyes from water by transition metal oxides: a review, Appl. Surf. Sci. Adv. 15 (2023) 100395, https://doi.org/10.1016/j.apsadv.2023.100395.

[7] M.Q. Gubari, H.M. Zwain, W.H. Hassan, M. Vakili, A. Majdi, Desalination of pigment industry wastewater by reverse osmosis using OPM-K membrane, Case Studies in Chemical and Environmental Engineering 8 (2023) 100401, https://doi.org/10.1016/j.cscee.2023.100401.

[8] O. Eskikaya, Z. Isik, C. Arslantas, E. Yabalak, D. Balakrishnan, N. Dizge, K.S. Rao, Preparation of Hydrochar bio-based catalyst for Fenton process in dye-containing wastewater treatment, Environ. Res. 216 (2023) 114357, https://doi.org/10.1016/j.envres.2022.114357.

[9] M. Zhang, S. Qin, Y. Tan, Z. Shen, QSAR model and microscopic mechanism analysis of dye removal by coagulation of aluminum chloride under alkaline conditions, Front. Environ. Sci. 11 (2023) 1156150, https://doi.org/10.3389/fenvs.2023.1156150.

[10] M.A. Al-Nuaim, A.A. Alwasiti, Z.Y. Shnain, The photocatalytic process in the treatment of polluted water, Chem. Pap. 77 (2) (2023) 677–701, https://doi.org/10.1007/s11696-022-02468-7.

[11] A. Bassi, P. Kalakonda, I. Hasan, Synthesis of chitosan-agar immobilized NiO-MgO bionanocomposites and their photocatalytic application towards toxic azo dye, Inorg. Chem. Commun. 170 (2024) 113499, https://doi.org/10.1016/j.inoche.2024.113499.

[12] P. Kalakonda, R. Kathi, M.G. Ligory, N. Dabbeta, N. Madipoju, S. Mynepally, V. Morampudi, S. Banne, P. Mandal, R.N. Savu, S.J. Khanam, M. Banavoth, N.V. Sudarsanam Eve, B.B. Podila, Argyreia Nervosa-driven biosynthesis of cu–ag bimetallic nanoparticles from plant leaves extract unveils enhanced antibacterial properties, Bioprocess Biosyst. Eng. 47 (8) (2024) 1307–1319, https://doi.org/10.1007/s00449-024-03020-5.

[13] M.R. Hoffmann, S.T. Martin, W. Choi, D.W. Bahnemann, Environmental applications of semiconductor Photocatalysis, Chem. Rev. 95 (1) (1995) 69–96, https://doi.org/10.1021/cr00033a004.

[14] N.K. Madipoju, S.J. Khanam, G. Sunkari, S.M. Vasamsetti, V. Divyasri, V. Morampudi, R.N. Savu, M. Banavoth, S. Banne, I. Hasan, P. Kalakonda, Bimetallic zinc-silver nanocomposites for superior antimicrobial efficacy, Appl. Phys. A Mater. Sci. Process. 131 (2) (2025) 153, https://doi.org/10.1007/s00339-025-08289-1.

[15] M. Anjum, R. Miandad, M. Waqas, F. Gehany, M.A. Barakat, Remediation of wastewater using various Nano-materials, Arab. J. Chem. 12 (8) (2019) 4897–4919, https://doi.org/10.1016/j.arabjc.2016.10.004.

[16] K.K. Senapati, C. Borgohain, P. Phukan, CoFe2O4–ZnS nanocomposite: a magnetically recyclable Photocatalyst, Cat. Sci. Technol. 2 (11) (2012) 2361, https://doi.org/10.1039/c2cy20400b.

[17] A. Anwar, M. Imran, M. Ramzan, F.A. Khan, N. Ismail, A.I. Hussain, S.M. Hussain, W.F. Alsanie, H.M.N. Iqbal, Chitosan-based Dy2O3/CuFe3O4 bio-nanocomposite development, characterization, and drug release kinetics, Int. J. Biol. Macromol. 220 (2022) 788–801, https://doi.org/10.1016/j.ijbiomac.2022.08.119.

[18] S.B. Vipparla, N. Debbata, S. Dharmapuri, A.K. Busi, P.B. Kalakonda, D. Aitipamula, M. Kigozi, P. Mandal, K.K. Balu, P. Kalakonda, Sustainable water purification using green-synthesized nanoparticles: a comparison between mono- and bimetallic nanoparticle systems, Asia Pac. J. Chem. Eng. 21 (1) (2026) e70144, https://doi.org/10.1002/apj.70144.

[19] J.M. Gonçalves, L.V. De Faria, A.B. Nascimento, R.L. Germscheidt, S. Patra, L.P. Hernández-Saravia, J.A. Bonacin, R.A.A. Munoz, L. Angnes, Sensing performances of spinel ferrites MFe2O4 (M = Mg, Ni, Co, Mn, Cu and Zn) based electrochemical sensors: a review, Anal. Chim. Acta 1233 (2022) 340362, https://doi.org/10.1016/j.aca.2022.340362.

[20] D.H.K. Reddy, Y.-S. Yun, Spinel ferrite magnetic adsorbents: alternative future materials for water purification? Coord. Chem. Rev. 315 (2016) 90–111, https://doi.org/10.1016/j.ccr.2016.01.012.

[21] M. Sumalatha, P. Nagaraju, M.S. Reddy, Review on spinel cobalt ferrites: cutting-edge applications, Phys. Scr. 101 (14) (2026) 142001, https://doi.org/10.1088/1402-4896/ae58fd.

[22] J.A. Oyetade, O.A. Iresemowo, M.I. Adeoba, O.E. Fayemi, S.F. Abimbade, A.O. Adeeyo, Functional impacts of carbon-based nanomaterials in the performance of heterostructure photocatalysts for the remediation of pharmaceutical pollutants in wastewater- a review, Nano-Structures & Nano-Objects 46 (2026) 101675, https://doi.org/10.1016/j.nanoso.2026.101675.

[23] S.L. N, K. S, T. Abisheik, V. Pandiyan, A.K. Alanazi, A. Raja, P. Kalakonda, A. Thirumurugan, G. Sandoval-Hevia, K. Balu, Urea-mediated Tb-TiO2 nanocomposites for azo dyes breakdown stimulated by UV and solar light: a smart solution for wastewater detoxification and microbial control, Surf. Interfaces 76 (2025) 107909, https://doi.org/10.1016/j.surfin.2025.107909.

[24] G. Sunkari, S. Vijaylakshmi, M. Sowjanya, S.M. Vasamsetti, N.K. Madipoju, N.K. Dabbeta, P. Kumar, P.B. Kalakonda, L.C. Kalakonda, V. Morampudi, S. Jammalamadaka, P. Kalakonda, Synergistic antibacterial activity of green-synthesized ag-Fe-Zn trimetallic nanocomposites using Tinospora Cordifolia leaf extract, Materials Chemistry and Physics: Sustainability and Energy 5 (2025) 100048, https://doi.org/10.1016/j.macse.2025.100048.

[25] H.-Z. Zhang, S. Kasibhatla, J. Kuemmerle, W. Kemnitzer, K. Ollis-Mason, L. Qiu, C. Crogan-Grundy, B. Tseng, J. Drewe, S.X. Cai, Discovery and structure–activity relationship of 3-Aryl-5-Aryl-1,2,4-Oxadiazoles as a new series of apoptosis inducers and potential anticancer agents, J. Med. Chem. 48 (16) (2005) 5215–5223, https://doi.org/10.1021/jm050292k.

[26] M. Nagaraju, S. Chandra Sekhar, S. Junied Arbaz, J. Su Yu, Solvothermal-derived nanoscale spinel bimetallic oxide particles rationally bridged with conductive vapor-grown carbon fibers for hybrid supercapacitors, Appl. Surf. Sci. 563 (2021) 150223, https://doi.org/10.1016/j.apsusc.2021.150223.

[27] A. Lu, E.L. Salabas, F. Schüth, Magnetic nanoparticles: synthesis, protection, functionalization, and application, Angew. Chem. Int. Ed. 46 (8) (2007) 1222–1244, https://doi.org/10.1002/anie.200602866.

[28] Q.Y. Tamboli, S.M. Patange, Y.K. Mohanta, R. Sharma, K.R. Zakde, Green synthesis of cobalt ferrite nanoparticles: an emerging material for environmental and biomedical applications, J. Nanomater. 2023 (2023) 1–15, https://doi.org/10.1155/2023/9770212.

[29] N.K. Dabbeta, M. Kante, R. Konda, A. Devarala, P.B. Kalakonda, S.J. Khanam, R.N. Savu, M. Banovath, L.S.R. Siddey, V.N. Bommaji, Eco-inspired Cu-Zn bimetallic nanoparticles for enhanced water purification technologies, Materials Chemistry and Physics: Sustainability and Energy 2 (2025) 100013.

[30] A.J. Driscoll, N. Bhat, R.A. Karron, K.L. O'Brien, D.R. Murdoch, Disk diffusion bioassays for the detection of antibiotic activity in body fluids: applications for the pneumonia etiology research for child health project, Clin. Infect. Dis. 54 (suppl_2) (2012) S159–S164, https://doi.org/10.1093/cid/cir1061.

[31] B. Kowalska-Krochmal, R. Dudek-Wicher, The minimum inhibitory concentration of antibiotics: methods, interpretation, clinical relevance, Pathogens 10 (2) (2021) 165, https://doi.org/10.3390/pathogens10020165.

[32] S.K. Jaganathan, A. Mazumdar, D. Mondhe, M. Mandal, Apoptotic effect of eugenol in human Colon Cancer cell lines, Cell Biol. Int. 35 (6) (2011) 607–615, https://doi.org/10.1042/CBI20100118.

[33] B. Emmanuel, S. Thomas, G. Raghuvaran, D. Sherwood, Simulated XRD profiles of carbon nanotubes (CNTs): an efficient algorithm and a recurrence relation for Characterising CNTs, J. Alloys Compd. 479 (1–2) (2009) 484–488, https://doi.org/

10.1016/j.jallcom.2008.12.109.
[34] Z. Ahmad, A. Khalid, Z.M. Aldhafeeri, I. Barsoum, E.G. Hanna, M. Hasan, A. Anwar, M. Aadil, Fine-tuning of redox-ability, optical, and electrical properties of Bi2MoO6 ceramics via lanthanide doping and rGO integration for photo-degradation of methylene blue and ciprofloxacin, J. Alloys Compd. 1002 (2024) 175466, https://doi.org/10.1016/j.jallcom.2024.175466.
[35] R.M. Silverstein, G.C. Bassler, Spectrometric identification of organic compounds, J. Chem. Educ. 39 (11) (1962) 546, https://doi.org/10.1021/ed039p546.
[36] R.M. Silverstein, F.X. Webster, D.J. Kiemle, D.L. Bryce, Spectrometric Identification of Organic Compounds, Eighth edition, Wiley, Hoboken, NJ, 2015.
[37] N.U.A. Khakwani, M. Aadil, I. Barsoum, Z. Ahmad, G.M. Kamal, M.R. Karim, A.A. Alothman, M.F. Warsi, Tailoring the physical, optical, and structural properties of bismuth oxide to enhance its anionic, cationic, and phenol dye degradation activities, Ceram. Int. 50 (18) (2024) 33333–33344, https://doi.org/10.1016/j.ceramint.2024.06.143.
[38] P.C. Ma, B.Z. Tang, J.-K. Kim, Effect of CNT decoration with silver nanoparticles on electrical conductivity of CNT-polymer composites, Carbon 46 (11) (2008) 1497–1505, https://doi.org/10.1016/j.carbon.2008.06.048.
[39] M.M. Sotoudehnia, A. Paúl, Dispersion of carbon nanotubes in iron by wet processing for the preparation of iron–carbon nanotube composites, Powder Technol. 258 (2014) 1–5, https://doi.org/10.1016/j.powtec.2014.03.006.
[40] C. Zhang, B.-Q. Chen, Z.-Y. Li, Y. Xia, Y.-G. Chen, Surface plasmon resonance in bimetallic core–shell nanoparticles, J. Phys. Chem. C 119 (29) (2015) 16836–16845, https://doi.org/10.1021/acs.jpcc.5b04232.
[41] R.C.F.G. Lopes, B.G.M. Rocha, E.M.S. Maçôas, E.F. Marques, J.M.G. Martinho, Combining metal nanoclusters and carbon nanomaterials: opportunities and challenges in advanced Nanohybrids, Adv. Colloid Interf. Sci. 304 (2022) 102667, https://doi.org/10.1016/j.cis.2022.102667.
[42] H. Pan, Y.P. Feng, Semiconductor nanowires and nanotubes: effects of size and surface-to-volume ratio, ACS Nano 2 (11) (2008) 2410–2414, https://doi.org/10.1021/nn8004872.
[43] J. Naseem, Mohamed.A. Rafea, M.E.A. Zaki, M.I. Attia, Mohamed.R. El-Aassar, F. Alresheedi, S. Zulfiqar, M. Aadil, Combining nanotechnology and nanohybrid methods to improve the physical and chemical properties of CuS and boost its photocatalytic aptitude, RSC Adv. 15 (18) (2025) 13940–13950, https://doi.org/10.1039/D5RA00602C.
[44] H.C. Kang, W.H. Weinberg, Structure of a Langmuir-Hinshelwood reaction Interface, Phys. Rev. E 48 (5) (1993) 3464–3469, https://doi.org/10.1103/PhysRevE.48.3464.
[45] J. Wang, G. Wang, B. Cheng, J. Yu, J. Fan, Sulfur-doped g-C3N4/TiO2 S-scheme heterojunction Photocatalyst for Congo red Photodegradation, Chin. J. Catal. 42 (1) (2021) 56–68, https://doi.org/10.1016/S1872-2067(20)63634-8.
[46] A. Khan, H.-Y. Chen, C. Rusly, Visible-light-driven removal of mixed dye pollutants by a novel ZnO/CNT/GO ternary nanocomposite: synergistic degradation of Congo red and methylene blue, Environ. Res. 283 (2025) 122156, https://doi.org/10.1016/j.envres.2025.122156.
[47] M. Azzi, I. Laib, A. Bouafia, I. Medila, A. Tliba, S.E. Laouini, H. Alsaeedi, D. Cornu, M. Bechelany, A. Barhoum, Antimutagenic and anticoagulant therapeutic effects of Ag/Ag2O nanoparticles from *Olea europaea* leaf extract: mitigating Metribuzin-induced hepato-and nephrotoxicity, Front. Pharmacol. 15 (2024) 1485525.
[48] H.A. Kouser, E.V. Kumar, V. Kamat, H.S.B. Naik, Photocatalytic degradation phenomena of methylene blue dye by ZnFe2O4 decorated with rGO nanocomposites under visible light irradiation, Next Nanotechnology 9 (2026) 100342, https://doi.org/10.1016/j.nxnano.2025.100342.
[49] S. Hussain, Md. Mottahir Alam, M. Imran, M. Ashraf Ali, T. Ahamad, A.S. Haidyrah, S.M.A. Raji Alotaibi, M. Naik, M. Shariq, A facile low-cost scheme for highly photoactive Fe3O4-MWCNTs nanocomposite material for degradation of methylene blue, Alex. Eng. J. 61 (11) (2022) 9107–9117, https://doi.org/10.1016/j.aej.2022.02.050.
[50] H.-S. You, S.-J. Ryu, H.-Y. Lee, J.-S. Baek, Enhanced antibacterial activity of multi-walled carbon nanotubes loaded with hot-melt extruded mulberry leaf silver nanoparticles, Colloids Surf. A Physicochem. Eng. Asp. 699 (2024) 134522, https://doi.org/10.1016/j.colsurfa.2024.134522.
[51] N. Sanpo, C.C. Berndt, C. Wen, J. Wang, Transition metal-substituted cobalt ferrite nanoparticles for biomedical applications, Acta Biomater. 9 (3) (2013) 5830–5837, https://doi.org/10.1016/j.actbio.2012.10.037.
[52] F. Bray, M. Laversanne, H. Sung, J. Ferlay, R.L. Siegel, I. Soerjomataram, A. Jemal, Global cancer statistics 2022: GLOBOCAN estimates of incidence and mortality worldwide for 36 cancers in 185 countries, CA Cancer J. Clin. 74 (3) (2024) 229–263, https://doi.org/10.3322/caac.21834.
[53] A.S. Ahmed, I.F. Waheed, Preparation of CNFO@g-C_3N_4-K magnetic nanocomposite for dual Photodegradation of methylene blue and carbon dioxide adsorption, Surf. Interfaces 82 (2026) 108524, https://doi.org/10.1016/j.surfin.2026.108524.
[54] E.M.S. Azzam, N.A. Fathy, S.M. El-Khouly, R.M. Sami, Enhancement the photocatalytic degradation of methylene blue dye using fabricated CNTs/TiO2/AgNPs/surfactant nanocomposites, J. Water Process Eng. 28 (2019) 311–321, https://doi.org/10.1016/j.jwpe.2019.02.016.